

Interaction of ultrashort laser pulses with metal nanotips: a model system for strong-field phenomena

This article has been downloaded from IOPscience. Please scroll down to see the full text article.

2012 New J. Phys. 14 085019

(<http://iopscience.iop.org/1367-2630/14/8/085019>)

View [the table of contents for this issue](#), or go to the [journal homepage](#) for more

Download details:

IP Address: 130.183.90.175

The article was downloaded on 27/09/2012 at 15:12

Please note that [terms and conditions apply](#).

Interaction of ultrashort laser pulses with metal nanotips: a model system for strong-field phenomena

Michael Krüger¹, Markus Schenk¹, Peter Hommelhoff^{1,3},
Georg Wachter², Christoph Lemell^{2,3} and Joachim Burgdörfer²

¹ Max Planck Institute of Quantum Optics, Hans-Kopfermann-Strasse 1,
D-85748 Garching, Germany

² Institute for Theoretical Physics, Vienna University of Technology,
Wiedner Hauptstrasse 8-10, A-1040 Vienna, Austria

E-mail: peter.hommelhoff@mpq.mpg.de and lemell@concord.itp.tuwien.ac.at

New Journal of Physics **14** (2012) 085019 (16pp)

Received 2 March 2012

Published 22 August 2012

Online at <http://www.njp.org/>

doi:10.1088/1367-2630/14/8/085019

Abstract. We discuss the interaction of ultrashort near-infrared laser pulses with sharp metal tips at moderate nominal intensities ($I_0 \sim 10^{11} \text{ W cm}^{-2}$). As external electric fields are strongly enhanced at such tips (enhancement factor ~ 10) our system turns out to be an ideal miniature laboratory to investigate strong-field effects at solid surfaces. We analyse the electron-energy spectra as a function of the strength of the laser field and the static extraction field and present an intuitive model for their interpretation. The size of the effective field acting on the metal electrons can be determined from the electron spectra. The latter are also reproduced by time-dependent density functional theory (TDDFT) simulations.

³ Authors to whom any correspondence should be addressed.

Contents

1. Introduction	2
2. Experimental methods and results	3
3. The simple man's model for nanotips	6
4. Time-dependent density functional theory simulations	11
5. Conclusions	15
Acknowledgments	15
References	15

1. Introduction

The emerging field of attosecond science is based on the ability to control electronic wavepackets with the help of well-controlled few-cycle laser pulses [1]. The key effect is the recollision of an electronic wavepacket with the parent matter within a fraction of the laser cycle after its generation through ionization [2, 3]. Prominent dynamical processes based on recollision are high-harmonic generation (HHG) and high-order above-threshold ionization (ATI), observed with atomic and molecular gases. The exquisite control over the recolliding wavepacket allows one to take, for example, diffraction images of the parent molecule [4, 5] and to achieve attosecond time resolution for electronic processes [6–8]. Recently, laser–electric-field-driven recollision processes were also observed with solid-state systems, namely at dielectric nanoparticles [9] and at sharp metal tips [10, 11].

For versatile imaging techniques applied to atomic, molecular and solid-state systems it would be of great interest to vary the parameters of the returning electron over a large energy range. The same holds true in the process of the generation of high-harmonic photons, which is currently being optimized to match certain flux and energy requirements (see, e.g., [12, 13]). Improving and extending the ability to control the motion of the electronic wavepacket requires additional control knobs for the strong fields driving the wavepacket. One obvious choice would be the addition of a static (dc) electric field. Theory suggests [14–16] that the application of relatively small static fields, one to four orders of magnitude weaker than the maximum laser field, already leads to a modification of the path of the recolliding wavepacket and, hence, to changes of the resulting HHG spectrum. For example, the maximum HHG energy could be tripled if a static field with a field strength 10% that of the maximum laser field was applied [16]. Although considerably smaller than the amplitude of the moderately strong laser itself, application of such a (macroscopic) static field with a strength of a fraction of a GV m^{-1} is unfeasible, rendering this control tool exceedingly difficult to employ in laser–atom or laser–molecule interactions.

When nanostructures are irradiated with laser light, optical field enhancement takes place. The laser electric field is substantially enhanced in the vicinity of the surface of structures smaller than the wavelength. An important class of nanostructures are nanotip electron emitters [17]. Here optical field enhancement factors of about 10 notably alleviate the requirements on the laser system for strong-field photoemission experiments [10, 11, 18, 19]. Enhanced laser electric fields of the order of 0.02 au (10 GV m^{-1}) and more have been reached experimentally with gold and tungsten nanotips. As an additional benefit, high static electric fields are easily achievable and facilitate conceptionally simple imaging techniques of the

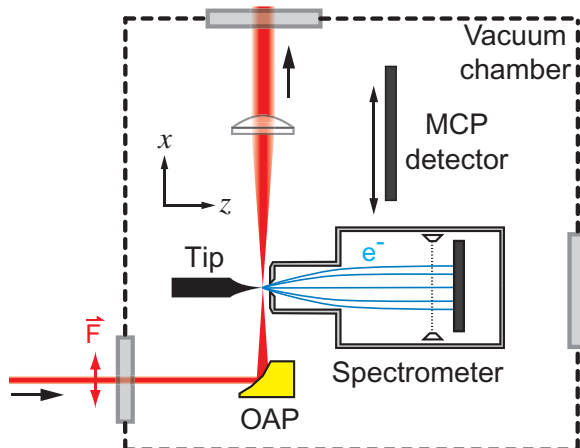


Figure 1. Setup for nanotip-based photoemission experiments. Laser pulses from a Ti:sapphire oscillator are tightly focused on a tungsten tip with an off-axis parabolic (OAP) mirror. Photoelectrons are detected either with an MCP detector that provides spatial resolution or with a retarding field spectrometer.

emitter surface by virtue of field emission microscopy (FEM) [20] and field ion microscopy (FIM) [21], the latter with atomic resolution.

Laser–nanotip interactions are therefore ideally suited for exploring the influence of additional static electric fields. In the following, we explore both experimentally and theoretically the influence of a superimposed dc field on the formation of the photoelectron spectrum and the plateau, the hallmark of rescattering of a strongly driven electron wavepacket. For a tungsten tip the experimentally observed electron spectrum can be surprisingly well ‘synthesized’ by a remarkably simple model which can be viewed as the extension of the well-known simple man’s model (SMM) to the nanotip geometry. It turns out that, despite the apparent complexity of the target, the SMM for nanotips (SMMN) is conceptionally simpler than for atoms or molecules due to the effective reduction of the dynamically relevant degrees of freedom.

2. Experimental methods and results

The experimental setup is described in detail in [19], so we only give a brief overview here. In our experiment, ~ 6.5 fs (full-width at half-maximum (FWHM) intensity) laser pulses generated by a Ti:sapphire oscillator at a repetition rate of 80 MHz are tightly focused on the apex of a sharp tungsten tip (see figure 1). In this experiment, the carrier–envelope phase (CEP) of the laser pulses is *not* stabilized and therefore random from pulse to pulse. CEP effects as reported in [10] are not the main focus of this investigation. The tip is fabricated from a single crystal tungsten wire in (310) crystallographic orientation. The radius of curvature at the tip apex is about $r \approx 8$ nm as determined from FIM images with the ring counting method [21]. The typical dimensions of the tip apex are hence much smaller than the focal spot size of ~ 2.4 μ m ($1/e^2$ intensity radius) and the central laser wavelength of 800 nm, so we expect optical field enhancement to occur at the tip surface.

Two interchangeable electron detectors can be used, a micro-channel plate (MCP) detector and a retarding field spectrometer. The MCP detector gives access to high-magnification

stereoscopic imaging of the electron emission sites and of the atomic structure of the tip surface with the FEM and FIM techniques. If the retarding field spectrometer is placed in front of the tip, energy spectra of electrons emitted in the forward direction can be recorded. In this case, the tungsten tip is grounded and the entrance aperture of the spectrometer is biased with a positive extraction voltage U . This potential difference gives rise to an electric field of magnitude

$$F_{\text{dc}} = -\frac{U}{kr} \quad (1)$$

at the surface of the tip apex. Equation (1) differs from the field at the surface of a charged sphere with radius r only by the dimensionless field reduction factor k . k accounts for the deviation of the shape of the tip from a sphere (mainly the tip's shank) and for the presence of the detector located at a distance d [21]. k is difficult to determine accurately because the shape of the tip apex is not precisely known.

The voltage-to-field conversion factor kr can be deduced from the field emission characteristics of the tip. For this purpose we record the field emission current J as a function of extraction voltage U with the spectrometer. Field emission follows the Fowler–Nordheim (FN) equation (see, e.g., [20, 22]). It is of the form

$$J(F_{\text{dc}}) \propto \frac{1}{t^2(y)} F_{\text{dc}}^2 \exp \left\{ -\frac{4\sqrt{2}}{3} v(y) \frac{W^{3/2}}{|F_{\text{dc}}|} \right\}, \quad (2)$$

where W is the metal work function and $y = \sqrt{|F_{\text{dc}}|}/W$ is the Nordheim parameter. The dimensionless Nordheim functions $t(y)$ and $v(y)$ (see, e.g., [23]) both approach 1 as $y \rightarrow 0$. Measuring $J(U)$ and displaying the data in an $\ln(J/U^2)$ versus $1/U$ plot (so-called FN plot) approximately yields a straight line with a slope s corresponding to the argument of the exponential function in equation (2). The factor kr can then be determined from s and equation (2) by

$$kr = -\frac{3}{4\sqrt{2}} \cdot \frac{s}{v(y) W^{3/2}}. \quad (3)$$

From measurements of the field emission current $J(U)$ performed before and after spectral measurements we deduce $kr = (162 \pm 11)$ nm with $W = 4.5$ eV and $v(y) = 0.77 \pm 0.04$. The latter value of $v(y)$ was deduced with the help of an iterative scheme [24]: we start with the assumption $v(y) = 1$, calculate a (preliminary) factor kr with equation (3), then determine F_{dc} from the average voltage U used to record the FN plot and finally calculate the Nordheim parameter y and $v(y)$ and repeat this procedure until convergence. In spectral measurements we found, however, that the effective barrier height increases within an hour after cleaning the tip [10, 19], presumably due to adsorbates. If we perform the above-mentioned analysis an increased barrier height W_{eff} results in a lower value for kr and ultimately in a higher field magnitude for a given voltage U . From spectral measurements we extract roughly $W_{\text{eff}} \sim 6$ eV [10] that results in $kr = 105$ nm. Due to the uncertainty in W_{eff} we estimate that $kr = (125 \pm 40)$ nm.

A series of spectra was recorded for gradually increasing laser intensities $I_0 = \{0.55, 0.72, 0.89, 1.1, 1.3\} \times 10^{11} \text{ W cm}^{-2}$ at a fixed extraction voltage of $U = 50$ V, corresponding to a static electric field of $F_{\text{dc}} = -(8 \pm 2) \times 10^{-4} \text{ au}$ ($\sim -0.4 \text{ GV m}^{-1}$; figure 2). At the lowest laser intensity, above-threshold photoemission (ATP) peaks are observed on top of an overall exponential decay [19]. The first photon peak at energy $E \approx 5.6$ eV corresponds to 4-photon photoemission. For higher intensities a radical change takes place: at energies

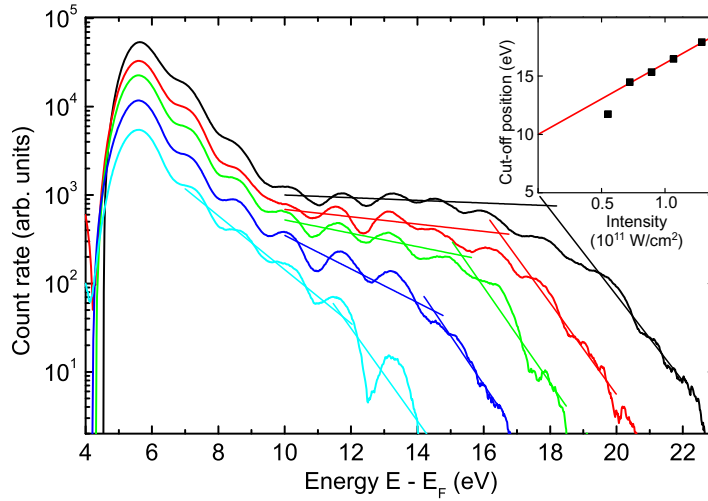


Figure 2. Photoelectron spectra for different laser intensities at a fixed extraction voltage $U = 50$ V ($F_{dc} = -0.4$ GV m $^{-1}$). From the bottom to the top, the curves are taken at nominal laser intensities $\{0.55, 0.72, 0.89, 1.1, 1.3\} \times 10^{11}$ W cm $^{-2}$. Energies are measured relative to the Fermi energy E_F . With increasing intensity, a plateau builds up at an energy $E > 9$ eV. It is more pronounced than the plateau reported in [11] because the static field strength $|F_{dc}|$ is smaller here (0.4 versus 0.7 GV m $^{-1}$). The tip radius is ~ 8 nm (in [11]: ~ 6 nm). Inset: cut-off position as a function of laser intensity (solid line: linear fit of the four data points with highest intensity). See the text for details.

$E > 9$ eV, a pronounced plateau structure builds up with increasing intensity. For the highest laser intensity measured, the count rate stays almost constant between 10 and 15 eV. It is more pronounced than the plateau reported in [11] because $|F_{dc}|$ is smaller here (-0.4 versus -0.7 GV m $^{-1}$, tip radii ~ 8 nm versus ~ 6 nm). The plateau structure is a hallmark of electron rescattering [25], here taking place at the surface of the metal tip [11]. Beyond the plateau part we observe a sharp drop-off of the count rate. This kink can be identified with the (classical) cut-off energy E_{cut} of rescattered electrons [3] and is given by the maximum kinetic energy a rescattered photoelectron can reach according to a classical description of electron propagation and scattering at the surface (in close analogy to the SMM for atoms [2]). An electron can reach a maximum kinetic energy of $E_{cut} = 10 U_p$, with U_p being the ponderomotive energy:

$$U_p = \frac{F_{eff}^2}{4\omega^2} = \frac{I_{eff}}{4\omega^2}. \quad (4)$$

U_p gives the mean quiver energy of an electron in a laser field of amplitude F_{eff} and photon energy ω . E_{cut} should therefore scale linearly with intensity I_{eff} . The intensity dependence of the position of the kink (inset of figure 2) confirms an approximately linear scaling and yields a slope of (6.1 ± 0.3) eV/ 10^{11} W cm $^{-2}$. Assuming the validity of $E_{cut} = 10 U_p + \text{const}$, however, yields a slope of 5.5 eV/ 10^{13} W cm $^{-2}$, indicating an intensity enhancement of more than two orders of magnitude or, equivalently, a field enhancement of about 10. This is corroborated by a numerical solution to the time-dependent Maxwell equations near nanotips, yielding an enhancement factor of the same order of magnitude (figure 3).

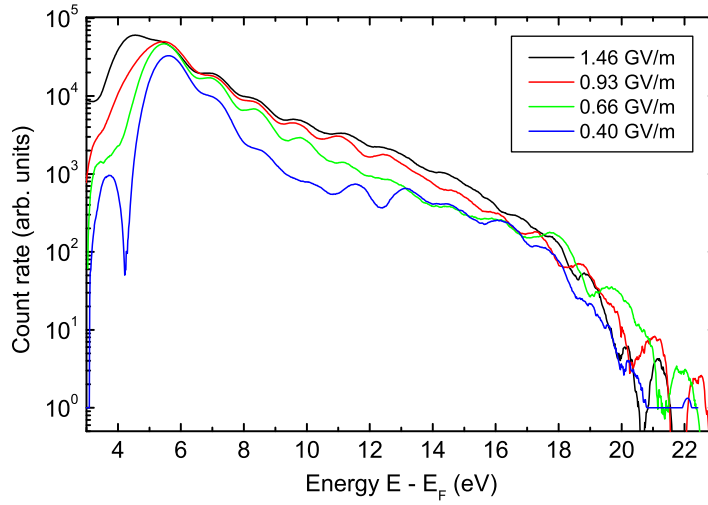


Figure 3. Photoelectron spectra for different static electric fields at a fixed nominal intensity $1.1 \times 10^{11} \text{ W cm}^{-2}$. The curves are taken at extraction voltages from 50 to 183 V, corresponding to effective electric field strengths at the tip from $F_{\text{dc}} = -0.78$ to $-2.8 \times 10^{-3} \text{ au}$ (from -0.4 to -1.5 GV m^{-1} , see the legend).

Unlike for atomic spectra it is now straightforward to experimentally explore the influence of a dc field on the ATP and plateau spectra by simply increasing the extraction voltage U . A series of spectra recorded at a fixed laser intensity of $I_0 = 1.1 \times 10^{11} \text{ W cm}^{-2}$ (nominal peak electric field $F_0 = 1.8 \times 10^{-3} \text{ au}$, not including field enhancement) for different voltages U corresponding to effective field strengths ranging from $|F_{\text{dc}}| = 0.78$ to $2.8 \times 10^{-3} \text{ au}$ (from -0.4 to -1.46 GV m^{-1}) reveals strong changes in the electron emission (figure 3).

Firstly, the spectral onset shifts to lower energies with an additional above-threshold photon peak becoming visible at energy $E \approx 4.5 \text{ eV}$. This results from the lowering of the surface barrier (Schottky effect [26]). In line with the Fowler–Nordheim theory [27] for field emission and assuming an asymptotic $-1/4z$ image potential superimposed on the static potential zF_{dc} , the lowering of the surface barrier height corresponds to

$$\Delta W(F_{\text{dc}}) = -\sqrt{|F_{\text{dc}}|}. \quad (5)$$

Secondly, the plateau becomes increasingly ‘tilted’ and is expected to eventually disappear for large F_{dc} . The cut-off energy E_{cut} of the plateau appears to be only weakly dependent on F_{dc} , with a slight shift towards lower energies as the field strength $|F_{\text{dc}}|$ increases.

3. The simple man’s model for nanotips

We present in the following a remarkably simple model that can account for the main qualitative features of the ATP and plateau formation in electron-emission spectra from laser-driven nanotips. This phenomenological description can be viewed as an extension of the SMM [28, 29] to the case of nanotips (SMMN) and possibly to other nanostructures as well. Despite the obvious complexity of the target compared to atoms in the gas phase, several specific geometric and dynamical features aid in the simplification such that the resulting model becomes even simpler than its atomic analogue. This fact underscores the notion that laser–nanotip interaction may serve as a testing ground for strong-field processes.

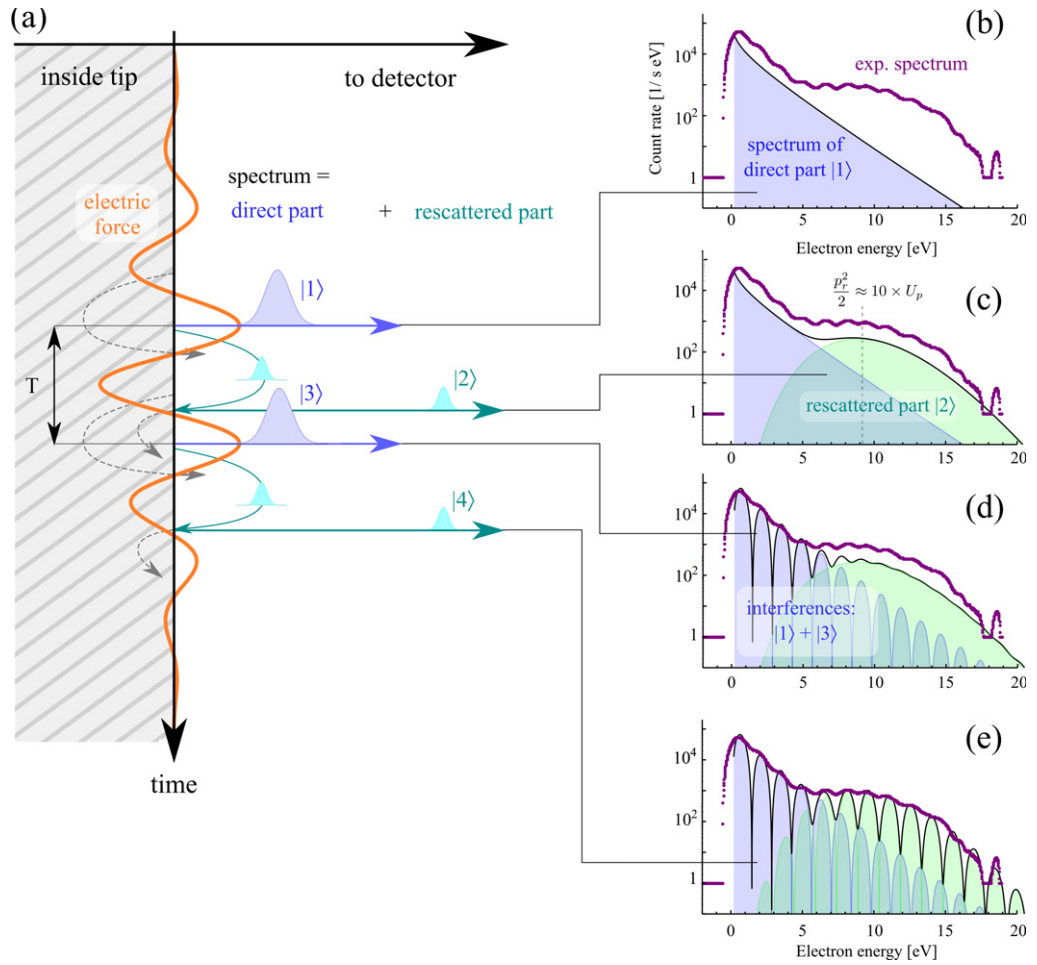


Figure 4. Sketch of the SMM for nanotips and the step-by-step formation of a typical spectrum. The laser electric force (orange) leads to emission of electrons near its maxima (large-amplitude wavepackets $|1\rangle$ and $|3\rangle$), generating the ‘direct’ spectrum (b). A fraction of the wavepackets returns to the surface and is backscattered, resulting in rescattered wavepackets with a larger central momentum (small-amplitude wavepackets $|2\rangle$ and $|4\rangle$; (c)). Repetition of these processes after multiples of one laser period T leads to interferences, that manifest themselves as ATP (see text).

One key ingredient is the locally enhanced electric field near the tip, which confines electron emission to the tip apex ($r \sim 10 \text{ nm} \ll \lambda = 800 \text{ nm}$). This region is still much larger than the characteristic length of the electron wave functions (Fermi wavelength $\sim 0.1 \text{ nm}$). Therefore, translational symmetry of the electron subsystem is approximately conserved in the surface plane, allowing for a quasi-one-dimensional treatment along the surface normal z with a spatially homogeneous laser field that includes field enhancement. In the following, we include enhancement into the effective electric field. Since the quiver amplitude at the driving wavelength and field strength is small compared to the spatial near-field decay profile of the enhanced field, its local variation is neglected. Another key feature is the effective screening of the driving field inside the solid ($z < 0$), leading to a drastic reduction of the number of paths to be included in the SMMN (figure 4(a)).

Accordingly, electrons are photoemitted by the laser electric field around the field maxima and driven away from the tip. A fraction of them will be driven back towards the surface as the laser electric field changes sign and are rescattered from the topmost atomic layer. These electrons reach higher kinetic energies and are responsible for the plateau and cut-off parts of the spectra. Interferences in the energy spectra develop due to the repetition of the process after multiples of the laser period T . These processes can be conveniently parameterized by a linear combination of Gaussian wavepackets for the direct and rescattered wavepackets.

The time-dependent Schrödinger equation in momentum space for a laser pulse in dipole approximation described in the velocity gauge by its time-dependent vector potential $A(t) = -\int_{-\infty}^t F(t')dt'$ reads

$$i\partial_t \phi(p, t) = \frac{(p + A(t))^2}{2} \phi(p, t), \quad (6)$$

where the instantaneous velocity (kinetic momentum) v is related to the (canonical) momentum p as $v = p + A(t)$. The time evolution of a wave function from time t_1 to time t_2 is accordingly given by the so-called Volkov propagator [30], which is diagonal in momentum space:

$$\psi(p, t_2) = \exp(-iS_p(t_2, t_1)) \psi(p, t_1), \quad (7)$$

where the Volkov phase

$$S_p(t_2, t_1) = \int_{t_1}^{t_2} \frac{1}{2} (p + A(t))^2 dt \quad (8)$$

is given by the classical action integral. Quantum–classical correspondence is invoked here on two different levels. First, according to Ehrenfest's theorem the time evolution of the expectation values of velocity and position

$$\langle v(t_2) \rangle = \langle v(t_1) \rangle - A(t_1) + A(t_2), \quad (9)$$

$$\langle x(t_2) \rangle = \int_{t_1}^{t_2} \langle v(t') \rangle dt' + \langle x(t_1) \rangle \quad (10)$$

follow the Newtonian equations of motion of a point charge in a laser field. Secondly, according to (7), the *individual momentum components* p of a wave function acquire a phase according to their time-dependent kinetic energy $v^2/2 = (p + A(t))^2/2$, which is that for a classical point charge following Newton's equations of motion (9).

It is instructive to analyse the terms contributing to the phase of the wave function according to the action integral (8) for a monochromatic vector potential, $A(t) = -(F_{\text{eff}}/\omega)\sin(\omega t)$:

$$S_p(t_2, t_1) = \left\{ \frac{p^2}{2} t + \alpha_q p \cos(\omega t) + U_p \left[t - \frac{1}{2\omega} \sin(2\omega t) \right] \right\} \Big|_{t_1}^{t_2}. \quad (11)$$

In addition to the first term associated with the energy, the momentum components acquire phases associated with the quiver motion of amplitude $\alpha_q = F_{\text{eff}}/\omega^2$ in the laser field as well as a constant and a time-dependent energy shift proportional to the average kinetic energy of an electron in a laser field, $U_p = (F_{\text{eff}}/2\omega)^2$.

For modelling electron emission and rescattering according to the SMM, we consider the time evolution of a Gaussian wavepacket launched at time t_1 with expectation value $p_1 = \langle p \rangle$ and momentum width σ_p ,

$$\psi_G(p, t, t_1) = e^{-(p-p_1)^2/4\sigma_p^2} e^{-iS_p(t, t_1)} e^{+i|W|t_1}, \quad (12)$$

where the Gaussian momentum spectrum is centred at the initial velocity $v_1 = p_1 + A(t_1)$. Prior to the emission at t_1 , the evolution of a bound state at the Fermi energy E_F is determined by the initial energy $-W$, while the subsequent time evolution is given by equation (7).

For tunnelling at an electric field maximum (direct part), we expect vanishing velocity at the tunnel exit and vanishing vector potential because the field is extremal so that $p_1 = 0$,

$$\psi_d(p, t, t_1) = e^{-p^2/4\sigma_p^2} e^{-iS_p(t, t_1)} e^{+i|W|t_1}, \quad (13)$$

and the associated momentum spectrum for this direct part after the end of the pulse is

$$|\psi_d(p)|^2 = e^{-p^2/2\sigma_p^2}, \quad (14)$$

leading to an exponentially decaying energy spectrum with a decay constant $1/\sigma_p^2$. An estimate of the longitudinal momentum distribution σ_p of emitted electrons for a given Keldysh parameter $\gamma = \sqrt{2W}\omega/F_{\text{eff}}$ has been given in [31]. It reduces to the ADK formula [32] in the tunnelling regime $\gamma \ll 1$:

$$P(p) = P_0 \exp(-p^2 c_1(\gamma)/\omega) \quad (15)$$

with

$$c_1(\gamma) = \text{Arcsinh}(\gamma) - \gamma(1 + \gamma^2)^{-1/2}. \quad (16)$$

Consequently, $\sigma_p^2 = \omega/2c_1(\gamma)$. The (effective) work function W entering the Keldysh parameter may become dependent on F_{dc} for strong static fields (see below). Inserting the experimental values for the work function ($W \simeq 4.5\text{--}6\text{ eV}$) and the effective electric field ($F_{\text{eff}} \simeq 0.02\text{ au}$ from the position of the cut-off, see below), we obtain for the width $\sigma_p \simeq 0.26\text{--}0.23$ in good agreement with the experimental spectrum of direct electrons (without rescattering) for the weakest extraction field of $\sigma_p = 0.225$ (figure 4(b)).

Subsequently, part of the emitted wavepacket is driven back to the surface when the laser field changes sign. We incorporate rescattering by making the approximation that all components of the wavepacket are elastically scattered at the same time t_2 , reversing the velocity (or kinetic momentum $p + A(t_2)$) $v(t_2) \rightarrow -v(t_2)$. This gives rise to a displacement of the wave function in momentum space

$$p(t = t_2 + \epsilon) = -p(t = t_2 - \epsilon) - 2A(t_2). \quad (17)$$

The Gaussian wavepacket ψ_r tunnelled at t_1 and reflected at t_2 reads

$$\psi_r(p, t, t_2, t_1) = e^{-[p+2A(t_2)-A(t_1)]^2/4\sigma_p^2} e^{+i|W|t_1} e^{-iS_{-p-A(t_2)}(t_2, t_1)} e^{-iS_p(t, t_2)}. \quad (18)$$

The momentum spectrum at the conclusion of the pulse is then

$$|\psi_r(p)|^2 = \exp(-(p + 2A(t_2) - A(t_1))^2/2\sigma_p^2), \quad (19)$$

a Gaussian with displaced average momentum

$$p_r = \langle \hat{p} \rangle = 2A(t_2) - A(t_1) \quad (20)$$

depending on the moment of emission and rescattering according to Newton's equation of motion (9). The classical cut-off energy derived in the SMM for atoms follows from maximizing (20) while constraining the rescattering time t_2 to times where the wavepacket emitted at t_1 is in the vicinity of the surface $\langle x(t_r) \rangle = 0$, yielding for a harmonic vector potential

$$p_r = \max(2A(t_2) - A(t_1))$$

$$p_r^2/2 = 10.0U_p \quad (21)$$

with optimal emission time $t_1 = 0.0415T$ and rescattering time $t_2 = 0.727T$.

Since the direct (d) and rescattered (r) portions of the wave function are well separated in momentum space, they can be added incoherently

$$|\psi(p)|^2 = |\psi_d(p)|^2 + |\psi_r(p)|^2 \quad (22)$$

without introducing a significant error. We note that for suitable pulse shapes the distance in momentum space between the direct and rescattered parts can be reduced, giving rise to additional interference effects. The resulting spectrum is shown in figure 4(c), showing already the plateau structure characteristic of rescattering. We note that our model predicts that the momentum width σ_p of the direct and rescattered wave functions is the same because there is no broadening process included. For the description of the experimental spectra, however, we find that the momentum width of the rescattered part is roughly by a factor of two larger than that of the direct part. Broadening could be accounted for by allowing for a distribution of rescattering times t_2 . Another broadening mechanism would be the energy dependence of the backscattering amplitude, which could be included into the model by multiplying (18) by a reflection amplitude $R(p) \exp(i\delta(p))$ with a scattering phase $\delta(p)$.

The characteristic peaks in the ATP spectrum of the direct part now follow from a coherent superposition of otherwise identical wavepackets launched at times t_j delayed relative to each other by multiples of the period T

$$\psi_d^{\text{ATP}}(p, t) = \sum_j c_{d;j} \psi_d(p, t, t_j). \quad (23)$$

For simplicity we restrict the sum in (23) to two terms (packets |1> and |3> in figure 4(a)). The total wave function for the direct part then reads (for simplicity assuming a maximum of the electric field at $t = 0$)

$$\psi_d^{\text{ATP}}(p, t) = c_{d;1} \psi_d(p, t, 0) + c_{d;2} \psi_d(p, t, T), \quad (24)$$

$$\psi_d^{\text{ATP}}(p, t) = e^{-p^2/4\sigma_p^2} (c_{d;1} e^{-iS_p(T,0)} + c_{d;2} e^{+i|W|T}) e^{-iS_p(t,T)}, \quad (25)$$

where the propagation after the ejection of the second wavepacket ($t > T$) only yields a global phase that drops out upon taking the absolute value. The corresponding momentum spectrum is, upon evaluating $S_p(T, 0)$ for the vector potential (11),

$$|\psi_d^{\text{ATP}}(p)|^2 = e^{-p^2/2\sigma_p^2} \left\{ c_{d;1}^2 + c_{d;2}^2 + 2c_{d;1}c_{d;2} \cos \left[\left(\frac{p^2}{2} + U_p + W \right) T \right] \right\}, \quad (26)$$

giving rise to ATP peaks at (figure 4(d))

$$E_{\text{kin}} + U_p + W = n\omega. \quad (27)$$

Analogously, the train of rescattered wavepackets yields a momentum spectrum

$$|\psi_r^{\text{ATP}}(p)|^2 = e^{-(p-p_r)^2/2\sigma_p^2} \left\{ c_{r;1}^2 + c_{r;2}^2 + 2c_{r;1}c_{r;2} \cos \left[\left(\frac{p^2}{2} + U_p + W \right) T \right] \right\} \quad (28)$$

with the same interference phase. We note that the precise value of the interference phase depends sensitively on the pulse shape (equation (11)). For short pulses the timing between

emission and rescattering of the rescattered wave function may change between bursts, leading to an additional phase shift and a time spacing between rescattered wavepackets that is slightly different from the laser period T in (28). In figure 4(e), the phase shift is $\sim\pi/6$ and the repetition time is $\sim 0.93 T$.

The resulting spectrum (figure 4(e))

$$|\psi^{\text{ATP}}(p)|^2 = |\psi_d^{\text{ATP}}(p)|^2 + |\psi_r^{\text{ATP}}(p)|^2 \quad (29)$$

resembles the experimental data amazingly well. It should be noted that the SMMN can be used to investigate the laser nanotip interaction along two different lines. One can either fit the experimental spectrum to equation (29) and deduce from the extracted value for p_r the effective field enhancement and, thereby, possibly even the tip geometry. In the present case, the fit to the data gives $p_r \approx 0.8$ and equation (21) implies $F_{\text{eff}} = 0.021$ au. Conversely, one can use the field enhancement as derived from the solution to Maxwell's equations near the tip, assuming a known geometry of the tip, and predict the spectrum via equations (21) and (29), thereby testing the ingredients of this elementary strong-field model. Its success hinges, in part, on the fact that, in contrast to ATI spectra from single atoms, fewer classes of trajectories contribute to the total spectrum due to broken symmetry at the metal surface. The laser field is strongly screened inside the solid (dashed grey lines in figure 4(a)). On the one hand, electrons that return to the surface but are not backscattered and enter the bulk experience no further significant interaction with the laser field and do not contribute to the total spectrum. On the other hand, there are no trajectories launched toward the inside of the solid. In laser-atom interactions, trajectories taking off during the same cycle in opposite directions give rise to intra-cycle interferences [33]. The reduction to only two types of trajectories for nanotip targets greatly simplifies the interpretation of electron-energy spectra.

It is now instructive to enquire into the effect of an additional static field F_{dc} as predicted by the SMMN outlined above. To leading order the static field will decrease the surface barrier height

$$W \rightarrow W(F_{\text{dc}}) = W - \sqrt{|F_{\text{dc}}|}. \quad (30)$$

This leads to a lowering of the threshold for photoemission (equation (27)) and to the appearance of an additional multi-photon peak below the zero-field threshold at $E \approx 4.5$ eV. In addition, through the dependence of the width of the longitudinal momentum distribution on W (equation (15)), the presence of a static field F_{dc} is expected to lead to a broadening of the tunnelling momentum distribution and to a reduced slope of the direct part of the spectrum. Finally, the SMMN predicts a (slight) decrease of the cut-off energy $E_{\text{cut}} \approx 10 (F_{\text{eff}} - |F_{\text{dc}}|)^2 / 4\omega^2$ since the presence of the dc field effectively reduces the kinetic energy and momentum of the returning electron at the moment of rescattering. All the predicted trends are in agreement with the experimental data.

4. Time-dependent density functional theory simulations

The phenomenological SMMN wavepacket model outlined above yields qualitative insight into the formation of the spectrum and provides estimates of parameter dependences in qualitative agreement with the experiment. Clearly, for a thorough understanding of the contributing processes a microscopic model incorporating the solid-state properties of the target is required.

We employ time-dependent density functional theory (TDDFT) [34–37] in one dimension, treating the coordinate along the surface normal z as the reaction coordinate. A detailed

description was given in [11]. Briefly, the time-dependent electron density $n(z, t)$ is expanded using the one-body Kohn–Sham pseudo wave functions $\psi_k(z, t)$

$$n(z, t) = \sum_{k=1}^{n_{\text{occ}}} a_k |\psi_k(z, t)|^2, \quad (31)$$

where $n_{\text{occ}} \approx 50$ is the number of occupied orbits up to the Fermi energy with weight coefficients a_k derived from the projection of the 3D Fermi sphere onto the tip axis [38]. Basic properties of the electron gas are determined by the Wigner–Seitz radius chosen as $r_s = 2.334$ au, giving a realistic Fermi energy of $E_F = 9.2$ eV. The width of the jellium slab is approximately 200 au. The time evolution of the electronic density is governed by the time-dependent Kohn–Sham equations

$$i\partial_t \psi_k(z, t) = \left\{ -\frac{1}{2} \partial_z^2 + V[n(z, t)] + V_{\text{ext}}(z, t) \right\} \psi_k(z, t). \quad (32)$$

The external potential due to the laser pulse is given in dipole approximation $V_{\text{ext}}(z, t) = zF_{\text{eff}}(t) + zF_{\text{dc}}$ where the laser field $F_{\text{eff}}(t)$ includes the field enhancement near the nanotip. $V[n(z, t)]$ contains the ground-state jellium potential and the response of the material to the external fields in terms of the electrostatic and exchange–correlation potentials. For the latter we assume the local density approximation (LDA) in the Perdew–Zunger parameterization [39]. To allow for rescattering at the atomic cores of the topmost target layer (i.e. the momentum reversal $v(t_2) \rightarrow -v(t_2)$) an additional potential simulating the atomic cores near the surface is added.

The time-dependent Kohn–Sham equations (32) are integrated in real space by the Crank–Nicolson method with a constant time step of 0.05 au up to a simulation time of typically 120 fs (~ 5000 au). The total size of the simulation box is 1425 au (9500 grid points) with absorbing boundary conditions to avoid unphysical reflections due to the finite size of the system. Electron emission spectra are determined [40] by a temporal Fourier transform of the wave functions at a computational detection point far from the surface (~ 900 au) in order to ensure that the laser pulse has terminated at the time of arrival of even the fastest electrons. Calculated spectra are broadened by 0.5 eV to match the experimental spectrometer resolution.

A typical result (figure 5) for the induced density fluctuations $\Delta n(z, t) = n(z, t) - n(z, t = -\infty)$ corresponding to experimental parameters (laser intensity $I_0 = 1.1 \times 10^{11} \text{ W cm}^{-2} \rightarrow F_{\text{eff}} = 0.02$ au, surface extraction field $F_{\text{dc}} = -1.9 \times 10^{-4} \text{ au} = -0.1 \text{ GV m}^{-1}$, pulse length (FWHM intensity) of 6.4 fs, photon energy $\hbar\omega = 0.057$ au and carrier–envelope phase $\phi_{\text{CEP}} = +\pi$) displays the ‘pulsed’ electron emission into vacuum ($z > 0$) near the field maxima (solid arrows). As the laser field changes sign, electrons are driven back towards the surface. They rescatter from the surface approximately at the zero crossings of the electric field (maxima of the vector potential, not shown), visible as interferences of steep slope (marked by dashed arrows). In this space–time plot, a large slope indicates high velocity representing high-energy electrons contributing to the plateau in the spectra. The fading of the density with increasing distance from the surface is due to the longitudinal spread of the wavepackets in time. The process repeats itself at subsequent field maxima. Even though the effective Keldysh parameter $\gamma_{\text{eff}} \approx 1.9$ (including field enhancement; the nominal γ_0 is even larger) is outside the tunnelling regime ($\gamma \ll 1$), emission bursts near the two central field maxima are clearly observable, qualitatively validating the SMMN wavepacket model. The time grating (or time double slit) leads to interferences in energy (multi-photon peaks), which are visible as interferences in the density plot.

Inside the tip ($z \leq 0$), the laser field induces density fluctuations that screen the external laser field. The induced density inside the solid is approximately two to three orders of

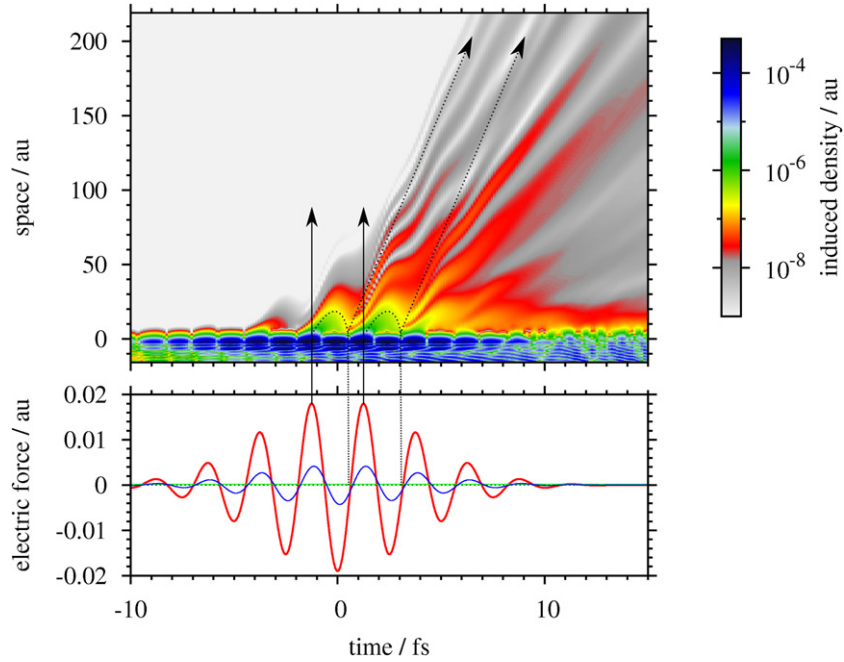


Figure 5. TDDFT sample simulation. Top panel: absolute value of the time-dependent induced electron density $n(z, t) - n(z, -\infty)$ (for comparison, the bulk density is $n_0 = 1.88 \times 10^{-2}$ au). The tip is located at $z \leq 0$. Bottom panel: time-dependent force exerted by the laser electric field (red) and the static field (green), and the induced dipole moment (blue, in arbitrary units). Emission happens mostly near the maxima of the electric field (vertical solid arrows). Electrons are subsequently driven back to the surface and rescatter (vertical dashed lines). Interferences in position space with increasing slopes (velocities) are detected as equi-spaced multi-photon peaks in the energy spectra (tilted arrows).

magnitude larger than the emitted part of the density but is still two orders of magnitude smaller than the bulk electron density $n_0 = 1.88 \times 10^{-2}$ au. Since on the electron time scale set by the Fermi momentum $k_F \approx 1$ au the laser field varies very slowly (period $T \approx 110$ au), this small fraction of the electron density can almost adiabatically adjust to the external field, screening it within a small surface layer of about 10 au. This is reflected in the induced dipole moment (blue line in figure 5), which is almost in phase with the driving field.

We now explore the dependence of the electron spectrum on laser intensity (or effective laser field strength F_{eff}) at a fixed extraction field F_{dc} (figure 6) and on extraction field strength at a fixed laser intensity (figure 7). In our simulation we average over eight different carrier-envelope phases since the CEP was not stabilized in the experiment. The build-up of a plateau (figure 6) with increasing laser amplitude at the tip varying from $F_{\text{eff}} = 0.008$ au to $F_{\text{eff}} = 0.021$ au (other laser parameters are the same as above) is clearly visible. From the comparison between the reference experimental spectrum (black dots) and the simulated spectra we can infer the effective peak field to be about $F_0 = 0.02$ au, in good agreement with the experimental estimate ($F_{\text{eff}} = 0.018$ au) and the fit to the data according to equation (21). Other features of the experimental data (threshold energy, slope of direct part, plateau and cut-off) are equally well reproduced.

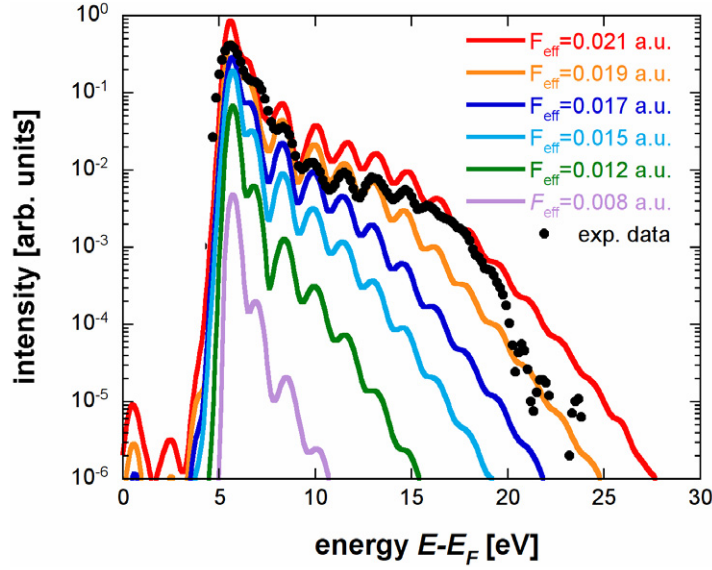


Figure 6. Simulated spectra for varying laser field strength F_{eff} from 0.008 to 0.021 au. Best agreement between experimental (black dots) and simulated data is found for $F_{\text{eff}} \approx 0.02$ au.

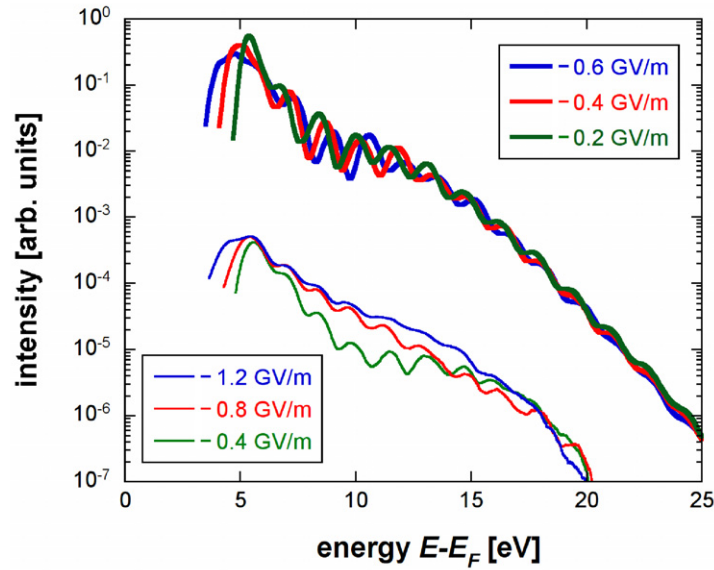


Figure 7. Comparison of simulated spectra (lines, upper graphs) and experimental results (thin lines, lower graphs) for varying static field F_{dc} , shifted vertically relative to each other for clarity.

The comparison between theory and experiment for varying static field strength F_{dc} (figure 7) reproduces the main features of the experiment and the predictions of the SMMN. In agreement with the data, the threshold moves to lower energies when the effective work function is reduced (the Schottky effect). The slope of the direct part is reduced with increasing static field because the momentum distribution of tunnelling electrons changes. The high-energy

cut-off, on the other hand, remains almost unchanged as long as the static field is much smaller than the laser amplitude.

The shift in the threshold energy allows for a quantitative comparison between experimental dc voltage and the simulated (enhanced) static field effective at the surface, F_{dc} . The best agreement is found for $F_{\text{dc}} = -0.2$ to -0.3 GV m^{-1} in good agreement with the experimental value of $F_{\text{dc}} \approx -(0.4 \pm 0.1) \text{ GV m}^{-1}$ for $U = 50 \text{ V}$.

In the plateau part of the spectrum, we observe, however, a qualitative difference between simulation and experiment. While in the experiment an increasing static field mainly reduces the visibility, in the simulation the main effect of an increased field is a shift in peak positions without a decrease in peak visibility. The origin of this difference remains to be investigated. We note that both of these effects should be sensitive to details of the phase of the electron wave functions near the surface.

5. Conclusions

We have both experimentally and theoretically investigated the electron emission spectrum in laser–nanotip interactions at nominally moderate laser intensities. Due to field enhancement near the nanotip this system has proved to be an excellent testing ground for strong-field phenomena. In particular, effects of the superposition of a dc field and the laser field can be conveniently demonstrated. We have shown that a model akin to the SMM for atomic and molecular targets can both qualitatively and quantitatively describe the electron spectrum remarkably well. For nanotips this model is, to a certain degree, conceptually even simpler than its atomic analogue because of the effectively reduced dimensions and the smaller number of effectively contributing paths. We have validated this SMMN by TDDFT simulations. Overall, we find surprisingly good agreement with experimental data considering the complexity of the target. Remaining discrepancies are likely related to oversimplifications of the surface potentials employed.

Acknowledgments

This work was supported by the Austrian Science Foundation (FWF) under project numbers SFB-041 ViCoM and P21141-N16. MS and GW thank the International Max Planck Research School of Advanced Photon Science for financial support. This work was partially supported by the European Union (FP7-IRG).

References

- [1] Krausz F and Ivanov M 2009 *Rev. Mod. Phys.* **81** 163
- [2] Corkum P B 1993 *Phys. Rev. Lett.* **71** 1994
- [3] Paulus G G, Becker W, Nicklich W and Walther H 1994 *J. Phys. B: At. Mol. Opt. Phys.* **27** L703
- [4] Niikura H, L  g  re F, Hasbani R, Bandrauk A D, Ivanov M Y, Villeneuve D M and Corkum P B 2002 *Nature* **417** 917
- [5] Baker S, Robinson J S, Haworth C A, Teng H, Smith R A, Chirila C C, Lein M, Tisch J W G and Marangos J P 2006 *Science* **312** 424
- [6] Schultze M *et al* 2010 *Science* **328** 1658

- [7] Nagele S, Pazourek R, Feist J, Doblhoff-Dier K, Lemell C, Tökesi K and Burgdörfer J 2011 *J. Phys. B: At. Mol. Opt. Phys.* **44** 081001
- [8] Lemell C, Solleder B, Tökesi K and Burgdörfer J 2009 *Phys. Rev. A* **79** 062901
- [9] Zherebtsov S *et al* 2011 *Nature Phys.* **7** 656
- [10] Krüger M, Schenk M and Hommelhoff P 2011 *Nature* **475** 78
- [11] Wachter G, Lemell C, Burgdörfer J, Schenk M, Krüger M and Hommelhoff P 2012 *Phys. Rev. B* **86** 035402
- [12] Popmintchev T, Chen M C, Arpin P, Murnane M M and Kapteyn H C 2010 *Nature Photonics* **4** 822
- [13] Serrat C and Biegert J 2010 *Phys. Rev. Lett.* **104** 073901
- [14] Bao M Q and Starace A F 1996 *Phys. Rev. A* **53** R3723
- [15] Lohr A, Becker W and Kleber M 1997 *Laser Phys.* **7** 615
- [16] Odžak S and Milošević D B 2005 *Phys. Rev. A* **72** 033407
- [17] Krüger M, Schenk M, Förster M and Hommelhoff P 2012 *J. Phys. B: At. Mol. Opt. Phys.* **45** 074006
- [18] Bormann R, Gulde M, Weismann A, Yalunin S V and Ropers C 2010 *Phys. Rev. Lett.* **105** 147601
- [19] Schenk M, Krüger M and Hommelhoff P 2010 *Phys. Rev. Lett.* **105** 257601
- [20] Fursey G 2005 *Field Emission in Vacuum Microelectronics* (New York: Kluwer)
- [21] Tsong T T 1990 *Atom-Probe Field Ion Microscopy* (Cambridge: Cambridge University Press)
- [22] Murphy E L and Good R H 1956 *Phys. Rev.* **102** 1464
- [23] Forbes R G 2006 *Appl. Phys. Lett.* **89** 113122
- [24] Gomer R 1961 *Field Emission and Field Ionization* (Cambridge, MA: Harvard University Press)
- [25] Paulus G G, Nicklich W, Xu H, Lambropoulos P and Walther H 1994 *Phys. Rev. Lett.* **72** 2851
- [26] Schottky W 1914 *Z. Phys.* **15** 872
- [27] Fowler R H and Nordheim L 1928 *Proc. R. Soc. Lond. A* **119** 173
- [28] Lewenstein M, Balcou P, Ivanov M Y, L'Huillier A and Corkum P B 1994 *Phys. Rev. A* **49** 2117
- [29] Lewenstein M, Kulander K C, Schafer K J and Bucksbaum P H 1995 *Phys. Rev. A* **51** 1495
- [30] Volkov D M 1935 *Z. Phys.* **94** 250
- [31] Popov V 1999 *JETP Lett.* **70** 502
- [32] Ammosov M, Delone N and Krainov V 1986 *Sov. Phys.—JETP* **64** 1191
- [33] Arbó D G, Persson E and Burgdörfer J 2006 *Phys. Rev. A* **74** 063407
- [34] Liebsch A 1997 *Electronic Excitations at Metal Surfaces* (New York: Plenum)
- [35] Burke K and Gross E K U 1998 *Density Functionals: Theory and Applications* (Berlin: Springer)
- [36] Maitra N T, Burke K, Appel H, Gross E K U and van Leeuwen R 2002 *A Celebration of the Contributions of Robert Parr* ed K D Sen (Singapore: World Scientific) pp 1186–225
- [37] Lemell C, Tong X M, Krausz F and Burgdörfer J 2003 *Phys. Rev. Lett.* **90** 076403
- [38] Eguluz A G 1983 *Phys. Rev. Lett.* **51** 1907
- [39] Perdew J P and Zunger A 1981 *Phys. Rev. B* **23** 5048
- [40] Pohl A, Reinhard P G and Suraud E 2000 *Phys. Rev. Lett.* **84** 5090